A Cavitied Cold Plate for Enhanced Thermal Uniformity and Cooling

Yanyan Liu, Sjouke Willem Schekman, Yongpu Wang, Tian Jian Lu, and Tongbeum Kim

***Abstract*—Excessive heat emitted from electronic and electrochemical devices, e.g., semiconductor chips and lithium (Li)-ion batteries, has been managed by a state-of-the-art technology—liquid circulation through designed (e.g., serpentine) microchannels embedded in a thin metallic "cold plate." Nonetheless, a common drawback of such thermal management technology is thermal nonuniformity. Even a small thermal gradient, for example, can accelerate performance degradation within a Li-ion battery cell. To mitigate such thermal nonuniformity, this study presents a novel cold plate design with enhanced cooling by placing hemicircular cavity cells along serpentine microchannels—namely, a cavitied cold plate. To demonstrate the design effectiveness, a series of thermofluidic characterizations on both the reference and cavitied cold plates subjected to constant heat flux are carried out by infrared (IR) thermography, as well as pressure and velocity measurements in a practical Reynolds number range of $20 \leq \mathrm{Re}_{Dh} \leq 200$. It is demonstrated that the proposed cavitied cold plate provides an improvement in thermal uniformity of ~70% over the reference one. This significant improvement is attributed to increased effective conductance by both elevated local convection and a shortened conductive path in cavity cells. Furthermore, the cavitied cold plate gives rise to more than 76% enhanced cooling, with 30% reduced pressure drop. Hence, with pumping power fixed, approximately 100% enhanced cooling over the reference cold plate could be achieved.**

***Index Terms*—Advanced cold plate design, battery/electronic chip cooling, serpentine microchannel, sidewall modification.**

I. Introduction

FOR effective thermal management of high-power electrical systems, one possible approach is forced convection of liquid coolant circulating through multiple serpentine microchannels embedded within a thin metallic plate, termed a "cold plate." Consider, as an example, lithium (Li)-ion batteries implemented in most electric vehicles (EVs) to date. Such a commercial battery pack is shown schematically in Fig. 1(a). The battery cooling system, shown in Fig. 1(b), features a metallic cold plate sandwiched between two prismatic battery cells that removes excessive heat from the battery cells via conduction. This is followed by forced liquid circulation through multiple serpentine microchannels in each cold plate. A pump drives the coolant circulation to carry the removed heat away and rejects it to the surroundings at the other end of the cooling system, where fins and air cooling are typically situated for heat rejection. At present, limited by the scale of the microchannels, the operating Reynolds numbers in such individual microchannels are $\mathrm{Re}_{Dh} \sim 100$ [1]. In general, a practical range of Reynolds numbers for microchannels is considered to be $20 \leq \mathrm{Re}_{Dh} \leq 200$ [2], and thus, the flows are characteristically "laminar."

The generation of electricity within Li-ion batteries involves chemical exothermic reactions, and hence, a thermal rise is inevitable. Excessive temperatures can rapidly cause significant capacity loss [3], [4]. Over and above the management of temperatures experienced by the batteries, temperature distribution across the battery cells is also essential [5], [6]. Nonuniform cooling could lead to hotspots. Cooling and regulation of such hotspots, in turn, result in regions receiving excess, inefficient levels of cooling. Therefore, the ultimate design goal for an efficient high-performance cold plate is enhanced cooling by convection in embedded microscale channels and more uniform thermal distribution, altogether with a lower pumping power requirement [7].

To improve the cooling performance of microchannel configurations, several modifications to the channels have been considered, including changes to surface roughness [8], [9], [10], curved flow path [11], [12], [13], and obstructions along the coolant flow direction [14], [15]. However, these techniques are all accompanied by an increase in pressure drop (i.e., pumping power). On the other hand, to improve the thermal uniformity in a cold plate, the core strategy has been on regulating the coolant distribution by optimizing microchannel topologies. This includes variable pin fin density [16], variable microchannel width [17], [18] along the coolant flow circuit, double-layer microchannel structure with counter flow [19], and inlet–outlet location arrangement (counter flow in adjacent microchannels) [20], [21]. Via these strategies, the thermal uniformity of a cold plate, considered based on a standard deviation of the surface temperature, could be improved by 22%~131%, depending on the reference cold

Received 3 April 2025; revised 31 May 2025 and 6 July 2025; accepted 6 July 2025. Date of publication 10 July 2025; date of current version 21 January 20256.This work was supported in part by the National Natural Science Foundation of China under Grant 12032010; and in part by the Postgraduate Research and Practice Innovation Program of Jiangsu Province, China, under Grant KYCX20_0173. Recommended for publication by Associate Editor J. Weibel upon evaluation of reviewers' comments. *(Corresponding authors: Tian Jian Lu; Tongbeum Kim.)*

Yanyan Liu, Yongpu Wang, Tian Jian Lu, and Tongbeum Kim are with the MIIT Key Laboratory of Multifunctional Lightweight Materials and Structures, Nanjing University of Aeronautics and Astronautics, Nanjing 210016, China (e-mail: liuyanyan@nuaa.edu.cn; ypwang@nuaa.edu.cn; tjlu@nuaa.edu.cn; tongbeum.kim@nuaa.edu.cn).

Sjouke Willem Schekman is with the School of Mechanical, Industrial and Aeronautical Engineering, University of the Witwatersrand, Johannesburg 2000, South Africa (e-mail: sjouke.schekman@wits.ac.za).

Digital Object Identifier 10.1109/TCPMT.2025.3587326

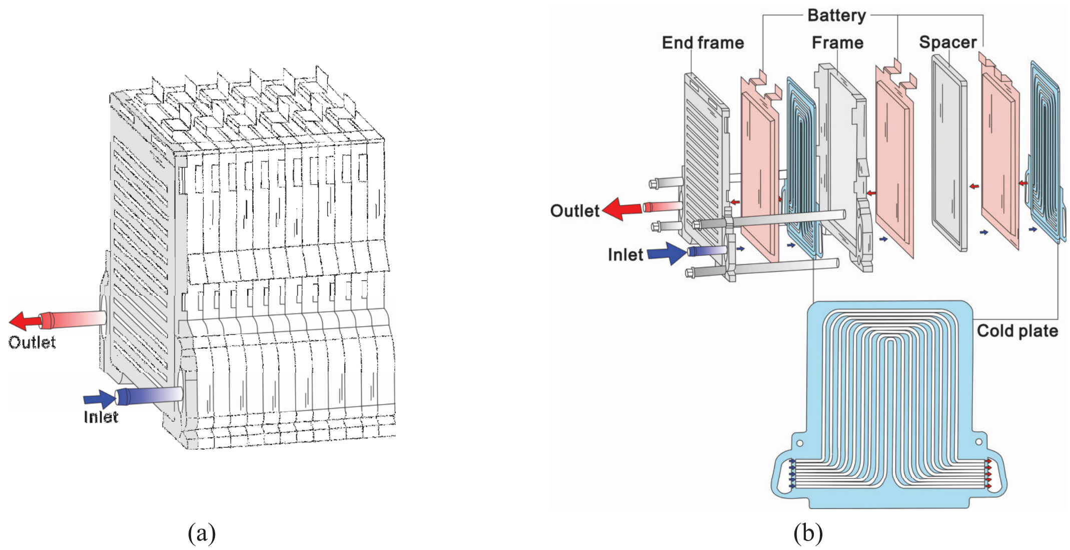

Fig. 1. Commercial prismatic Li-ion battery pack with a liquid cooling system [1], [2]. (a) Prismatic battery pack. (b) Sandwiched serpentine microchannel cold plates.

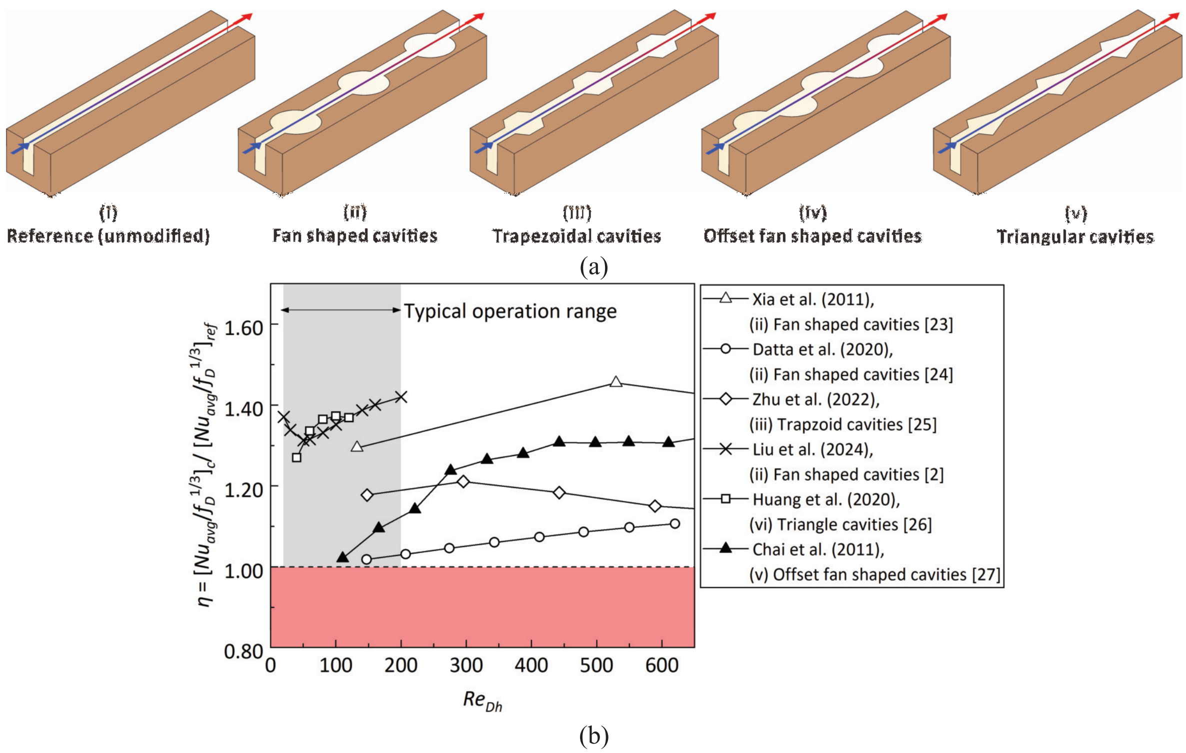

Fig. 2. Comparison of sidewall modifications in straight microchannels. (a) Sidewall modification configurations. (b) Thermal-hydraulic performance ratio.

plate used in individual studies. Notably, these modifications do not satisfy both requirements simultaneously—enhanced cooling and improved thermal uniformity.

A cold plate with sidewall modification, however, may meet both design requirements simultaneously as per the results in our previous studies [2], [22]. Specifically, the sidewalls of the microchannels are modified, creating cavities along the length of a channel, hitherto referred to as cavitied cold plates. Possible configurations of sidewall modification for single/multiple straight microchannel cold plates are shown in Fig. 2(a), including: (i) unaltered microchannel (reference); (ii) fan-shaped [2], [23], [24]; (iii) trapezoidal [25]; (iv) triangular [26]; and (v) offset fan-shaped [27] cavities. Such cavitied microchannels exhibit very interesting thermal-hydraulic properties. Enhanced cooling is achieved while reducing pressure drop compared to the unmodified microchannel [2]. The corresponding mechanisms have been stipulated in previous studies. It is attributed to the redeveloping boundary layers in the throat connecting successive cavities [2] and stagnant fluid within cavities [22]. The performance of a given microchannel

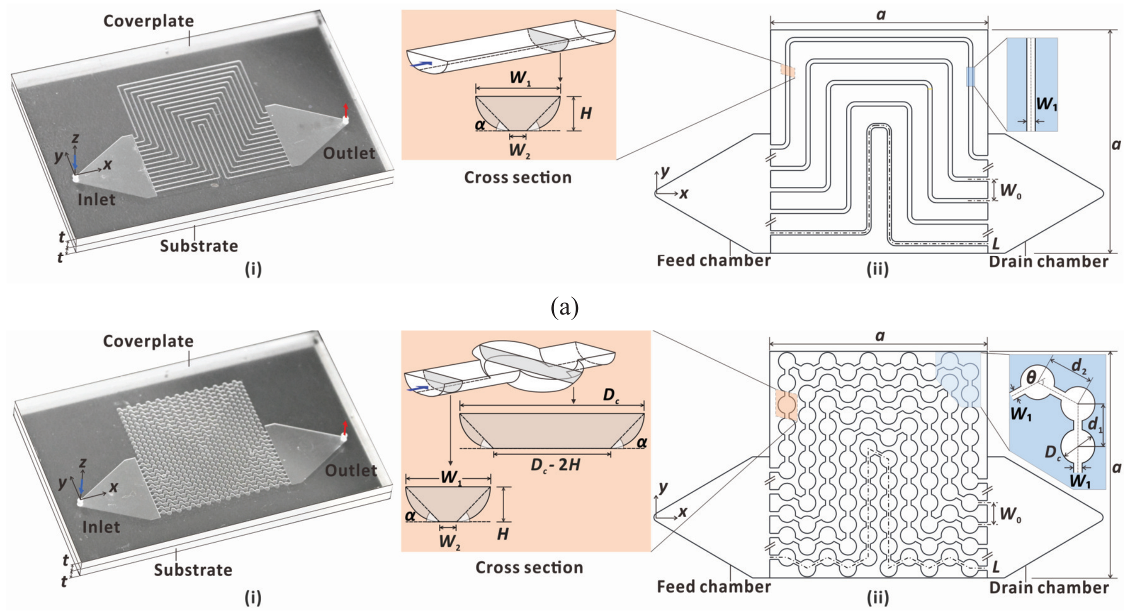

Fig. 3. Cold plate specimens showing a photograph of fabricated cold plates with schematic of designed microchannels. (a) Reference (unmodified) cold plate. (b) Cavitied cold plate.

can be measured through a thermal-hydraulic performance ($\mathrm{Nu}_{\mathrm{avg}}/f_D^{1/3}$), where $\mathrm{Nu}_{\mathrm{avg}}$ is the average Nusselt number and f_D is the friction factor. Furthermore, a thermal performance parameter, $\eta = [\mathrm{Nu}_{\mathrm{avg}}/f_D^{1/3}]_c/[\mathrm{Nu}_{\mathrm{avg}}/f_D^{1/3}]_{\mathrm{ref}} > 1.0$, represented in Fig. 2(b), implies a performance of cavitied (c) microchannels superior to reference (ref) microchannels at a given pumping power.

The design effectiveness in a practical configuration, i.e., a cold plate consisting of serpentine microchannels, is yet to be confirmed to enhance cooling and improve thermal uniformity simultaneously. Therefore, this study aims to squarely address this issue. To this end, a series of thermofluidic characterizations on both reference (unmodified) and modified metallic cold plates, subjected to a constant heat flux, are carried out by both infrared (IR) thermography and pneumatic pressure measurements in the Reynolds number range of $20 \leq R_{Dh} \leq 200$. Furthermore, to demonstrate detailed flow patterns within each cavity cell, microparticle image velocimetry (μPIV) is also employed, necessitating an optically transparent microchannel cold plate.

II. Materials and Methods

A. Microchannel Cold Plate Specimens

Two transparent rectangular-shaped microchannel cold plate specimens were fabricated, including a "reference" unmodified cold plate [Fig. 3(a)] and a cold plate with sidewall modification [Fig. 3(b)]. For both specimens, 13 predesigned microchannels were chemically etched out, via hydrogen fluoride, on a 2.0-mm-thick transparent quartz glass substrate within a 1×1 in (a = 25.4 mm) range. Another 2.0-mm-thick cover plate, which uses the same quartz glass as substrate, was press-fused on top of the substrate. The chemical etching resulted in a "bowl-shaped" cross-sectional shape as shown in the insets of Fig. 3. Upstream of and downstream from each microchannel passage, a wide-angle diffuser-type chamber was added to uniformly distribute a working fluid—deionized water—into the test passage. In this article, they were referred to as the feed chamber and the drain chamber. Geometrical dimensions of an individual microchannel were adopted directly from those used in [2] and [22]. This allowed for a more direct correlation to those previous findings as necessary. The dimensions were W_1 = 200 μm (top base), W_2 = 20 μm (bottom base), H = 90 μm (height), α = 45° (taper between the top and bottom bases), and L = 49.19 mm (total length), as indicated in Fig. 3(a). The center-to-center spacing between two adjacent microchannels was fixed at W_0 = 1000 μm. As for the proposed cavitied microchannel, 25 pairs of cavities with top diameter D_c = 800 μm were aligned along the straight microchannel passage in the y-axis, with center-to-center spacing fixed at d_1 = 1000 μm. Along the x-direction, the cavities were arranged in a staggered pattern, with center-to-center spacing fixed at d_2 = 1070 μm. The angle (θ) between the inlet and outlet of a cavity was 56°, resulting in a longer total flow path of L = 52.49 mm (Table I). For both reference and cavitied cold plates, L remains the same length from one microchannel to another.

B. Coolant Distribution in Both Types of Cold Plates

Prior to measurements, it is instructive to confirm that the coolant is distributed to multiple microchannels by a feed chamber. To this end, a series of flow visualizations were given in Fig. 4. For the Reynolds number of Re_{Dh} = 100, deionized water was first circulated using a syringe pump set at a targeted flow rate, and then, a red ink pigment was injected at the feed chamber.

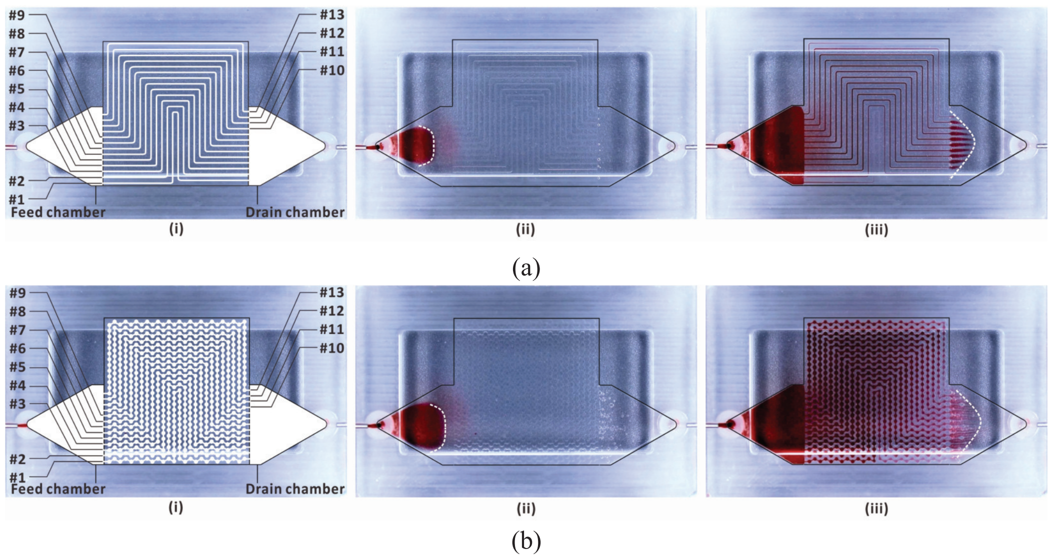

Fig. 4. Visualized coolant flow in a cold plate. (a) With unmodified sidewalls. (b) With cavitied sidewalls.

TABLE I

Geometric Parameters of Two Tested Glass Cold Plates With a Bowl-Shaped Cross Section

<table>
<tr><th rowspan="2">With 13 microchannels</th><th rowspan="2">a (mm)</th><th rowspan="2">t (mm)</th><th rowspan="2">L (mm)</th><th rowspan="2">$d_1 = W_0$ (μm)</th><th rowspan="2">D_c (μm)</th><th rowspan="2">d_2 (μm)</th><th rowspan="2">θ (°)</th><th colspan="5">Bowl-shaped cross-section</th><th rowspan="2">$A_{coolant}/a^2$</th></tr>
<tr><th>W_1 (μm)</th><th>W_2 (μm)</th><th>H (μm)</th><th>α (°)</th><th>D_h (μm)</th></tr>
<tr><td>Unmodified cold plate</td><td>25.4</td><td>2.0</td><td>49.19</td><td>1000</td><td>/</td><td>/</td><td>/</td><td rowspan="2">200</td><td rowspan="2">20</td><td rowspan="2">90</td><td rowspan="2">45</td><td rowspan="2">115.6</td><td>0.20</td></tr>
<tr><td>Cavitied cold plate</td><td>25.4</td><td>2.0</td><td>52.49</td><td>1000</td><td>800</td><td>1070</td><td>56</td><td>0.56</td></tr>
</table>

For both types of cold plates, the fluid entering the feed chamber forms a jet-like flow. Subsequently, the feed chamber flow enters the central microchannels (e.g., #5–#9) first since these are closer to the chamber inlet. No separation on the diverging sides of the feed chamber is observed (see (ii) of Fig. 4). When the coolant enters the drain chamber, after passing through all 13 microchannels, a similar distribution is maintained, with the flow exiting the central microchannels first (see (iii) of Fig. 4). This implies that, in both the reference and cavitied cold plates, the coolant is uniformly distributed by the wide-angle feed chamber as designed. Furthermore, no distinguishable differences are exhibited between the flow pattern in the unmodified microchannel system [Fig. 4(a)] and that in the cavitied microchannel system [Fig. 4(b)].

C. Time-Averaged Flow Field Measured With μPIV

The local flow field inside the transparent quartz microchannel with hemicircular cavitied sidewalls (as shown in Fig. 3) was mapped using a μPIV system, as schematically shown in Fig. 5. A Nd:YAG double-cavity pulsed laser (Evergreen 70, Lumibird) was used for illumination, which emitted two green laser pulses at 532-nm wavelength, with predefined time delay (t, $t+dt$). The laser beam was delivered into a stereo epi-fluorescent microscope (Stereo Discovery V8, Zeiss) passing the beam expander, which was then reflected, via a dichroic mirror, into the path perpendicular to the plane of a microscope objective lens. The beam expander employed was an optical component that became opaque when the laser beam intensity exceeded a certain limit, thus protecting the objective lens from damage [28], [29]. The laser beam coming out of the objective lens illuminated the entire measurement volume, including tracer particles and the microtube itself. However, the tracer particles were typically fluorescent, absorbing green light from laser beams and emitting longer wavelength fluorescent light. In these experiments, the tracer particles (2.0 μm in diameter and 0.01% volume concentration; Thermo Fisher Scientific) absorbed green laser light ($\lambda_0 \sim 532$ nm) and emitted orange, fluorescent light ($\lambda \sim 612$ nm). During preparation, the tracer particles were mixed with the DI water via ultrasonication (500-W Ultrasonic Processors, Cole-Parmer) for 60 s so that the former could be uniformly distributed in the latter.

Subsequently, the fluorescent light from tracer particles and the green light scattered by objects in the illumination volume were all transmitted back through the objective lens. However, a dichroic mirror was used to remove the green light reflected and scattered back into the objective lens. As the mirror only transmitted light in the range >610 nm, most of the fluorescent light from tracer particles passed through. It is worth noting that the dichroic mirror was the same as the one that reflected the illuminating laser beam into the objective lens. The signals from the measurement

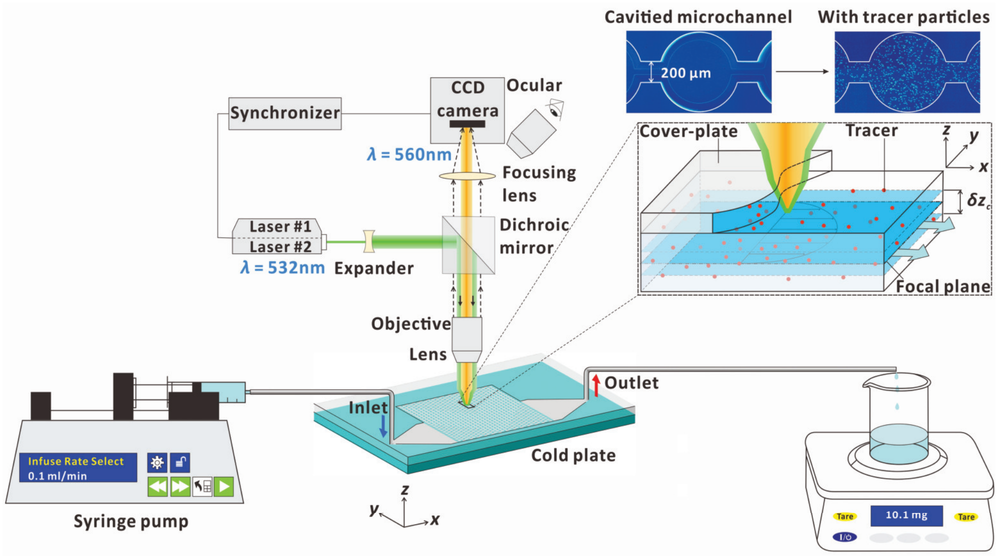

Fig. 5. Experimental setup for measuring local flow field using a μPIV system.

volume included the emitted lights from both the in-focus and out-of-focus particles, which were imaged using an interline transfer charge-coupled device (CCD) camera (Image SX 6M, LaVision). As shown in the enlarged inset of Fig. 5, the depth of correlation (δz_c) in the experiment was estimated to be ~33.5 μm, based on the following equation [30], [31]:

$$\delta z_c = 2\left[\frac{1-\sqrt{\varepsilon}}{\sqrt{\varepsilon}}\left(f^{\#^2} d_p^2 + \frac{5.95\,(M+1)^2\,\lambda^2 f^{\#^4}}{M^2}\right)\right]^{\frac{1}{2}} \quad (1)$$

where ε is the relative threshold below which the defocused particle images no longer contribute significantly to the displacement-correlation term (ε = 0.01 usually selected), $f^{\#}$ is the focal number of the lens, d_p is the tracer particle diameter, M is the magnification, and λ is the wavelength of the light emitted by tracer particles.

The double-shuttered CCD camera was used to record the light scattered by the particles, with double frame/double exposure. With time sequences adjusted by the synchronizer, the timing was such that the first laser pulse occurred in the first frame, whereas the second pulse occurred in the second frame. Both frames were subdivided into interrogation windows, with 96×96 pixels and 75% overlap. Each window was evaluated by cross correlation of the window in the first frame recorded at time instant t, with the same window in the second frame recorded at time instant $t + dt$. Velocity vectors could be obtained with a 16×16 pixel spatial resolution in a graphic user interface (DaVis 10, LaVision). Time-resolved data were recorded at a sampling rate of 8.0 Hz for 100 instantaneous velocity fields, which were averaged to obtain the time-averaged flow field.

To horizontally adjust the view windows and microscope focal plane, each cold plate specimen was fixed on a traverse system while keeping the flow field plane inside the microtube and the objective lens plane in a mutually parallel position. In all cases, velocity fields were measured along the microchannel mid-height plane, which was located by matching the maximum centerline velocity.

D. Steady-State Heat Transfer Measurements

To explore the forced convection performance of both unmodified and cavitied cold plates, two metallic cold plates with five purposely designed microchannels were fabricated, as shown in Fig. 6. These micropassages were machined using a microcomputer numerical control (Micro-CNC) on 0.5-mm-thick stainless steel 304 upper and lower substrates (k_s = 14.35 W/m·K). After machining, the two substrates were rebonded via diffusion welding. The two metallic cold plates had the same serpentine layout as their glass counterparts, as shown in Fig. 3. Therefore, the coolant is expected to be uniformly distributed into the test microchannels through the wide-angle feed chamber, as shown in Fig. 4.

For both types of metallic cold plates, the cross section of an individual microchannel was an ellipse (perimeter P = 2.17×10^3 μm and inner area A_c = 2.82×10^5 μm^2), slightly different from that of glass cold plates as seen in Fig. 6(c). This was unavoidable due to the different manufacturing processes employed for glass and metallic cold plates. However, it was not expected to significantly alter coolant flow behavior. The length of each microchannel was L = 50.36 mm, while the center-to-center spacing between two adjacent microchannels was fixed at W_0 = 2500 μm.

As for the cavitied microchannel, ten pairs of cavities with top diameter D_c = 2000 μm are aligned down the straight microchannel passage along the y-axis, with center-to-center spacing fixed at d_1 = 2500 μm. Along the x-direction, the cavities are arranged in a staggered manner, with center-to-center spacing fixed at d_2 = 2680 μm. The angle (θ) between inlet and outlet flowing through a cavity is 56°, resulting in a longer flow path L = 53.17 mm (Table II).

For steady heat transfer measurements, an etched foil heater with dimensions of 25.4×25.4 mm was attached to the back side of both metallic cold plates via a double-sided tape, as

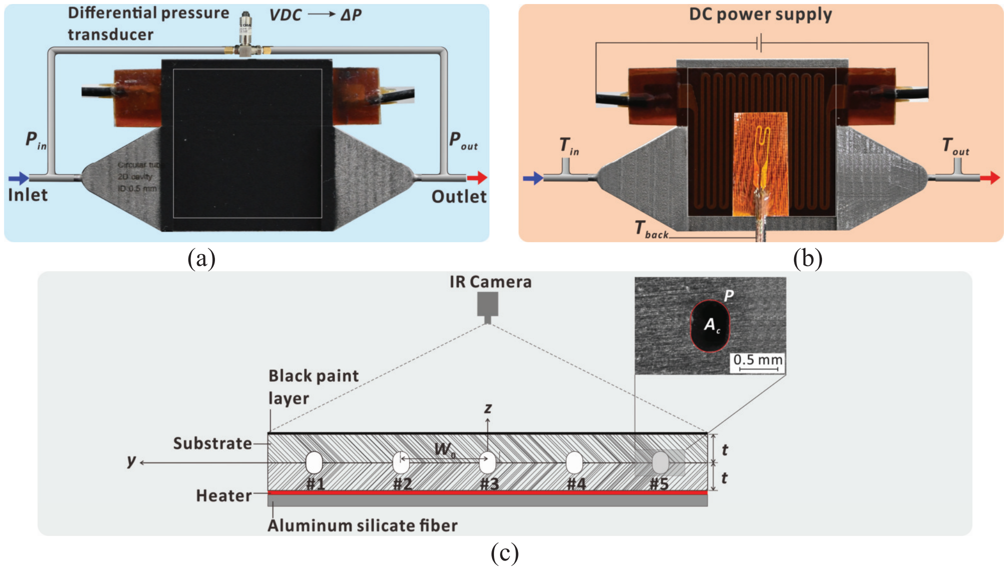

Fig. 6. Experimental setup for measuring steady-state heat transfer in a metallic microchannel cold plate. (a) Photograph from front side view. (b) Photograph from back side view. (c) Schematic of cross section.

TABLE II
GEOMETRIC PARAMETERS OF TWO TESTED METALLIC COLD PLATES WITH MICROCHANNELS HAVING ELLIPSE CROSS SECTIONS

With 5 microchannels	a (mm)	t (mm)	L (mm)	$d_1 = W_0$ (μm)	D_c (μm)	d_2 (μm)	θ (°)	Ellipse cross-section			$A_{coolant}/a^2$
								P (μm)	A_c (μm²)	D_h (μm)	
Unmodified cold plate	25.4	0.5	49.19	2500	/	/	/	2.17×10^3	2.82×10^5	520	0.20
Cavitied cold plate	25.4	0.5	52.49	2500	2000	2680	56°				0.53

shown in Fig. 6(b). To achieve the desired isoflux thermal condition, an electric current (with 10.0 V and 0.68 A from a dc power supply) was supplied, which generates an input heat of 6.8 W (corresponding input heat flux $q''_0 = 10.54$ kW/m^2) based on the heater area. The back side of the attached heater was thermally insulated with a sufficiently thick aluminum silicate fiber felt, as illustrated in Fig. 6(c). The current and voltage were measured using a digital multimeter.

Two T-type bead thermocouples (5TC-TT-T-40-36, Omega Engineering) were used to monitor inlet (T_{in}) and outlet (T_{out}) coolant temperatures through the tapping holes. Upon completing the heat transfer experiments, these tapping holes were also used to measure the pressure drop between the inlet and outlet ports. A T-type film thermocouple (CO1-T, Omega Engineering) was attached to the back side of the cold plate, as depicted in Fig. 6(b). Once the temperature (T_{back}) became stable, indicating steady-state forced convection within a given cold plate, an IR camera (Flir E8xt, FLIR[1]) was used to map surface temperatures on its top side. Emissivity of the top surface was taken to be 0.95 as estimated using the IR camera, by inversely matching temperature readings from the IR camera to those measured from the film thermocouple at the same location on the target plate. The time-resolved IR image was recorded at a sampling rate of 1.0 Hz for ten IR images, which were then averaged to obtain a time-averaged temperature contour on the top surface of each cold plate.

E. Time-Averaged Static Pressure Measurements

To measure time-averaged flow resistance (or pressure drop), a differential pressure transducer (PX409, Omega Engineering) was connected to two pressure tapping ports of each cold plate, with the latter connected to the inlet and outlet of the cold plate using a three-way valve [Fig. 6(a)]. This enabled pressure difference measurements at differing flow rates. The output signal of the differential pressure transducer was recorded by a data acquisition system (34972A, Keysight Technologies) at 20 Hz for 60 s, collecting 1200 sampled signals in total. The voltage signals were then converted and time-averaged to obtain the mean pressure drop for a given flow rate.

F. Data Reduction Parameters

Throughout the present study, the Reynolds number ranged from $20 \le \text{Re}_{Dh} \le 200$. For the microchannels specific to the present cold plate configurations, the hydraulic diameter was defined as follows:

$$D_h = \frac{4A_c}{P} \tag{2}$$

where A_c was the cross-sectional area and P was the cross-sectional perimeter for an individual microchannel. For the

[1]Trademarked.

bowl-shaped microchannel cold plate, $A_c = HW_2 + (\pi H^2)/2$, and $P = W_1 + W_2 + \pi H$. For the ellipse microchannel cold plate, the representative cross-sectional area and perimeter of individual microchannels were averaged from the values of five microchannels in the cold plate. The cross-sectional area and perimeter of each individual microchannel were measured using a commercial image processing program (ImageJ).

The Reynolds number (Re_{Dh}) was defined as

$$\mathrm{Re}_{Dh} = \frac{\rho u_m D_h}{\mu} \tag{3}$$

where ρ and μ were, respectively, the density and dynamic viscosity of distilled water and u_m was the mean velocity (setting value of the precalibrated syringe pump). The density and dynamic viscosities of distilled water at local temperature (25 °C) and barometric pressure (100 kPa) were 998.21 kg/m^3 and 1.0016×10^{-3} Pa·s, respectively.

As a nondimensional measure of flow resistance, the friction factor was calculated as

$$f_D = \left(\frac{2\Delta P}{L}\right)\left(\frac{1}{\rho u_m^2}\right) D_h \tag{4}$$

where ΔP was the pressure drop between the two pressure tapping ports of the specimen (measured by a differential pressure transducer) and L was the length of an individual microchannel.

To evaluate the forced convection performance of both cold plate types, the overall average Nusselt number was calculated as

$$\mathrm{Nu}_{\mathrm{avg}} = \frac{q''}{T_{s,m} - T_f}\frac{D_h}{k_f} \tag{5}$$

where $q'' = Q_{\mathrm{net}}/A_{\mathrm{interface}}$ was the average heat flux imposed on the surface of a microchannel, Q_{net} was the net power input, and $A_{\mathrm{interface}}$ was the microchannel interface area between the coolant and the solid substrate. $T_{s,m} = \sum_{j=1}^{y}\sum_{i=1}^{x} T_s(i,j)/(x \times y)$ was the mean value of top endwall temperature; $T_f = 0.5(T_{f,\mathrm{in}} + T_{f,\mathrm{out}})$ was the average temperature of coolant; and $T_{f,\mathrm{in}}$ and $T_{f,\mathrm{out}}$ were the coolant temperature at the inlet and outlet, respectively. $k_f = 0.6$ W/(m·K) was the thermal conductivity of DI water. The net power input was obtained via energy conservation as

$$Q_{\mathrm{net}} = c_p \dot{m}(T_{f,\mathrm{out}} - T_{f,\mathrm{in}}) \tag{6}$$

where c_p was the coolant thermal capacity and $\dot{m}$ was the mass flow rate.

Heat losses from the heater could thus be estimated as

$$R_{\mathrm{loss}} = \frac{Q_{\mathrm{input}} - Q_{\mathrm{net}}}{Q_{\mathrm{input}}} \tag{7}$$

where $Q_{\mathrm{input}} = UI$ was the power input from the heater and U and I were the voltage and current applied to the heater via a dc power supply, respectively. Depending upon individual setups, the magnitude of R_{loss} varied substantially, from 9% to 26% of the total heat input supplied to the heater.

The Nusselt number and friction factor reflect the heat transfer and flow resistance characteristics of the cavitied cold plate, respectively. The thermal-hydraulic performance [32], [33] at a fixed pumping power for a given microchannel, or performance evaluation criterion (PEC), is expressed as

$$\mathrm{PEC} = \mathrm{Nu}_{\mathrm{avg}}/f_D^{1/3}. \tag{8}$$

Furthermore, to evaluate the enhanced thermal-hydraulic performance of the cavitied cold plate compared to a reference unmodified cold plate, a thermal performance factor (η) was defined as

$$\eta = \left[\mathrm{Nu}_{\mathrm{avg}}/f_D^{1/3}\right]_c \Big/ \left[\mathrm{Nu}_{\mathrm{avg}}/f_D^{1/3}\right]_{\mathrm{ref}} \tag{9}$$

where subscripts "c" and "ref" denote the cavitied and reference cold plates, respectively. It expressed the ratio of the PEC of the cavitied cold plate to that of its reference counterpart.

To evaluate the thermal uniformity on the top surface of each cold plate, the standard deviation of the surface temperature was considered. It is considered that a smaller standard deviation of temperature implies a more uniform temperature distribution on the cold plate surface. This was expressed as

$$T_\sigma = \sqrt{\frac{1}{N}\sum_{i=1}^{N}\left(T_{s,i}(x,y) - T_{s,\mathrm{avg}}\right)^2} \tag{10}$$

where $T_{s,i}$ (x, y) was the temperature at each pixel of one IR image and $N = x \times y$ was the total pixel number of one IR image, T_s (x, y).

G. Uncertainty Analysis

Measurement uncertainties were estimated using a method described as follows. If $y = f(x_1, x_2, \ldots, x_n)$, then the uncertainty propagated by x_i in the variable y is given by [34]

$$\Delta y = \sqrt{\left(\frac{\partial y}{\partial x_1}\Delta x_1\right)^2 + \left(\frac{\partial y}{\partial x_2}\Delta x_2\right)^2 + \cdots + \left(\frac{\partial y}{\partial x_n}\Delta x_n\right)^2} \tag{11}$$

where Δx_i was the absolute uncertainty in x_i. Equation (11) estimated overall experimental uncertainties associated with mean velocity, Reynolds numbers, and friction factor. The uncertainty of mean velocity was associated with flow rate and cross-sectional area and was estimated to be 0.62%. Similarly, the estimated uncertainties of Reynolds number and pressure drop per unit length were within 0.86% and 1.00%, respectively. The uncertainty of the friction factor that was associated with the mean velocity, hydraulic diameter, and pressure drop per unit length was estimated to be less than 1.81%. Uncertainty of Nusselt number ($\mathrm{Nu}_{\mathrm{avg}}$) was associated with mean temperature on the top endwall ($T_{s,m}$), coolant's average temperature (T_f), and various heat losses during the experiment. This uncertainty was calculated as 9.28%, governed predominantly by uncertainty in input heat flux. Similarly, the estimated uncertainty of thermal uniformity (T_σ) is within 5.59%.

The uncertainty of the instantaneous velocity measured by μPIV is associated with the average particle displacement within an interrogation area and time interval of two frames. Uncertainty regarding the time interval of light sheet pulses is not usually considered to be a significant source of error. The displacement error is estimated based on the contributions of the random motion of tracer particles due to Brownian motion and implicit errors during interrogations. Santiago et al. [35] show that the error due to the Brownian motion of tracer particles is a function of the diffusion coefficient of microparticles, the characteristic velocity, and the time delay between successive images. The implicit errors during the interrogations could be estimated by particle image diameter (i.e., $d_\tau = 3.7$ pixels), the number of particle images (N_I) within the interrogation area, and subpixel displacements (ΔX) [36], [37], [38]. The total measurement uncertainty is determined to be $\pm 3.73\%$ based on the valid full-scale displacements of 5.0 pixels, where the random motion of tracer particles due to Brownian motion and implicit errors is combined by using the root sum square of these terms.

III. Results and Discussion

A. Enhanced Overall Cooling by Sidewall Modification

As a baseline (reference) case, the temperature distribution of each cold plate was considered without forced convection in its microchannels, i.e., $\mathrm{Re}_{Dh} = 0$. Temperatures thus measured for the reference case are displayed as contours (i) and (v) in Fig. 7(a) for the unmodified and cavitied cold plates, respectively. The temperature distribution is largely similar across both types of cold plates and akin to that temperature centered on a heat source. With $Q_{\mathrm{input}} = 6.8$ W applied to the bottom surface of the reference cold plate, the mean cold plate temperature, $T_{s,m} - T_{amb}$, was measured to be ~76.0 °C at $\mathrm{Re}_{Dh} = 0$.

The coolant at $T_{f,\mathrm{in}} = 25$ °C is now supplied to microchannels through a feed chamber, with Re_{Dh} varying from 20 to 200. Passing along the serpentine microchannels, the coolant removes heat and thus becomes hotter. As a result, the cooling effectiveness drops along the microchannel length: lower cold plate temperatures near the inlet and higher temperatures near the outlet. This is seen in contours (ii)–(iv) of Fig. 7(a) for the unmodified cold plate and in contours (vi)–(viii) for the cavitied cold plate.

For the unmodified cold plate, at $\mathrm{Re}_{Dh} = 60$, the hotspot extends from its center toward the outlet, as shown by contour (ii). As the Reynolds number is increased to 100, the hotspot migrates closer to the outlet, with a decreased peak temperature as depicted by contour (iii). As the Reynolds number is further increased to 200, the hotspot seems to disappear, yet with relatively higher temperature regions remaining along the inner side serpentine microchannels, as evidenced by contour (iv). Quantitatively, the mean surface temperature, by way of the temperature difference between the mean endwall temperature and the coolant inlet temperature ($T_{s,m} - T_{f,\mathrm{in}}$), drops steeply and monotonically, from ~33 °C to ~10 °C, as the Reynolds number is increased from 20 to 200.

For the cavitied cold plate, the variation of local temperature distributions and its dependence on Reynolds number are similar. However, the magnitude of surface temperatures is much lower than the reference cold plate, as evidenced by contours (vi)–(viii). In addition, unlike the unmodified cold plate, all microchannel paths have a higher temperature near the exit into the drain chamber, i.e., a better distribution of the temperature across the cold plate channels. The mean surface temperature ($T_{s,m} - T_{f,\mathrm{in}}$) is decreased steeply from ~20 °C to ~5 °C, which is much lower than the reference case, corresponding to between a 39.4% and 50% reduction in surface temperature. This confirms that a cavity-type sidewall modification has the potential to meet simultaneously the two design requirements of higher heat transfer and better cooling uniformity.

To better understand the dependence of forced convection in both cold plates on Reynolds number, the mean surface temperature (i.e., $T_{s,m} - T_{f,\mathrm{in}}$) was generalized by the Nusselt number ($\mathrm{Nu}_{\mathrm{avg}}$) defined in (5). The Nusselt number of the reference cold plate is seen to increase with increasing Reynolds number, as depicted in Fig. 7(b). This dependence seems contradictory to the classical theory that states that the Nusselt number is a constant ($\mathrm{Nu}_{\mathrm{theory}} = 4.36$, independent of Reynolds number), if cooled by fully developed laminar flow in a circular pipe subjected to constant heat flux [39].

The configuration considered in the present study, however, differs from that assumed in the classical derivation. Specifically, there is a strong thermal spreading in the substrate of the cold plate, along both the axial and transverse directions. This is termed "lateral spreading" in this study, referring to conduction through the substrate embedding the multiple serpentine microchannels. In an individual serpentine microchannel, there is both forced convection axially along the channel path and lateral spreading within the cold plate substrate. Previous studies [2], [40], [41], [42] that considered such thermal spreading in a straight microchannel cold plate argued that the imposed uniform heat flux on such a cold plate is redistributed. Consequently, the nonuniform heat flux along the microchannel surface causes a nonlinear variation of coolant temperature. The Nusselt number calculated using (5) is, therefore, underestimated.

On the other hand, as the Reynolds number is increased, lateral spreading becomes weakened relative to convective cooling. At sufficiently high Reynolds numbers, forced convection becomes dominant, with corresponding heat transfer eventually approaching the theoretical value of $\mathrm{Nu}_{\mathrm{theory}} = 4.36$, as depicted in Fig. 7(b). It should be noted that although (5) is strictly inaccurate, it still provides an alternative yet practical means to estimate the cooling performance of a given microchannel cold plate since it is almost impossible to experimentally measure local fluid temperature and heat flux along a microchannel [2], [40]. A direct comparison of $\mathrm{Nu}_{\mathrm{avg}}$ in Fig. 7(b) reveals that the cooling by the unmodified cold plate is increased from $\mathrm{Nu}_{\mathrm{avg}}$ ~ 0.34 to ~1.41 when the Reynolds number is increased from $\mathrm{Re}_{Dh} = 20$ to 200. On the other hand, for the cavitied cold plate, the Nusselt number is increased from $\mathrm{Nu}_{\mathrm{avg}}$ ~ 0.63 to ~2.10, which provides approximately 76% enhancement across the Reynolds number range considered.

Based on the results of Fig. 7, it can be concluded that to further enhance the cooling performance of a given cold plate design, the flow rate in the embedded microchannels should be increased. In such a case, the pumping of coolant is a critical design constraint where the pressure drop across these microchannels limits the permissible flow rate for a

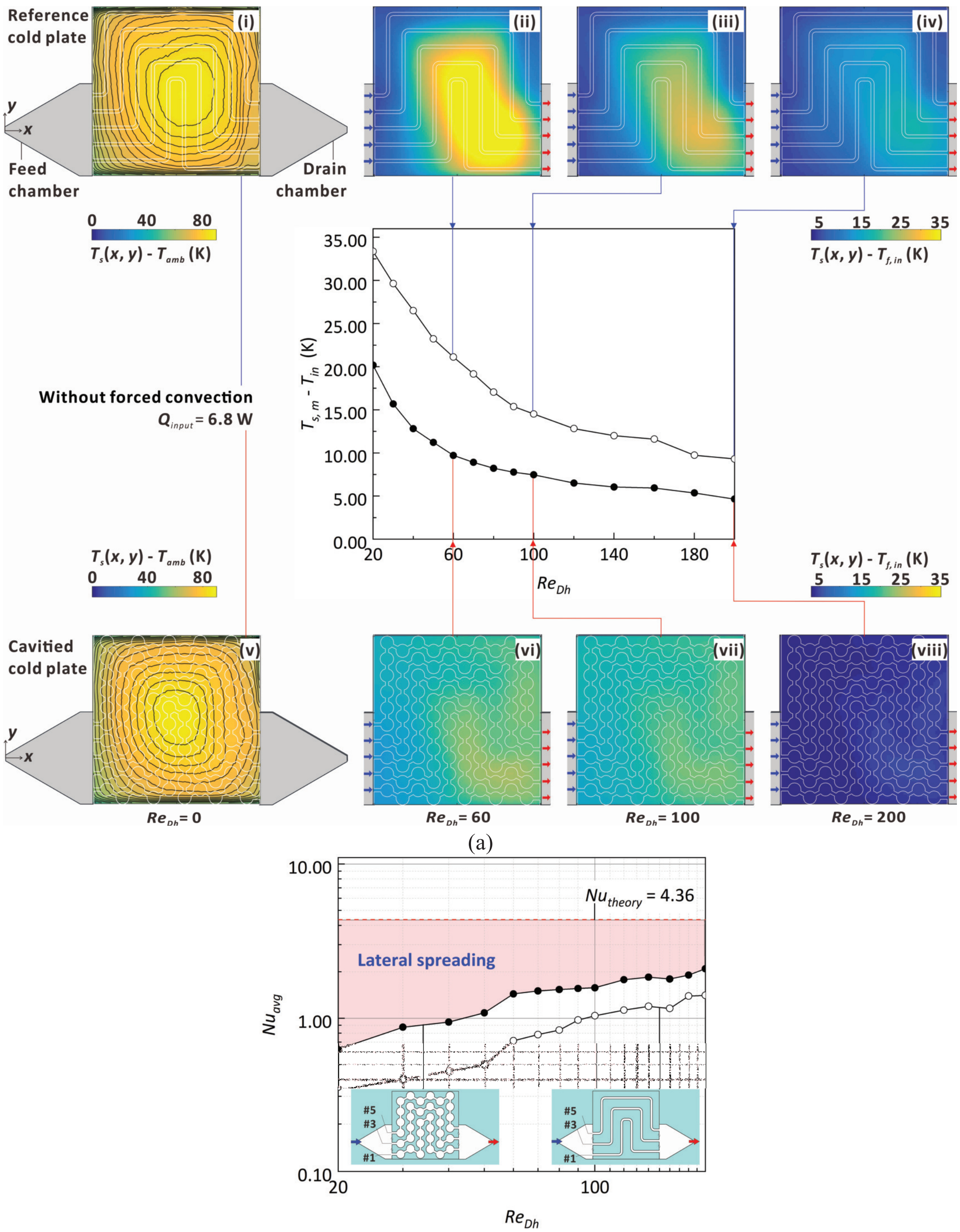

(a)

(b)

Fig. 7. Comparisons. (a) Cold plate surface temperature distribution and its variation with Reynolds number. (b) Area-averaged Nusselt number varying with Reynolds number.

given pump. Based on the Darcy–Weisbach equation [43], the pressure drop (ΔP) in a microscale channel is substantially higher than that in a macroscale channel, following a power law of $\Delta P \sim D^{-4}$, D being the hydraulic diameter of an individual coolant channel. In other words, microchannel systems require a more powerful pump.

For both cold plate types, Fig. 8(a) evaluates the pressure drop per unit length ($\Delta P/L$) varying with coolant mean velocity (u_m) from 0.04 up to 0.39 m/s. This velocity range corresponds to a Reynolds number range of Re_{Dh} = 20–200, which implies laminar flow convection. Pressure drop in the unmodified cold plate increases with the mean velocity as $\Delta P/L \sim (u_m)^{1.2}$, which is slightly steeper than the classical theory for laminar flow in a smooth pipe, e.g., $\Delta P/L \sim (u_m)^{1.0}$ [43]. Such a slight deviation may be attributed to the bends present along a serpentine microchannel [12]. With sidewall modification, the pressure drop increases with mean velocity to a lesser extent, following $\Delta P/L \sim (u_m)^{1.4}$. In the mean velocity range

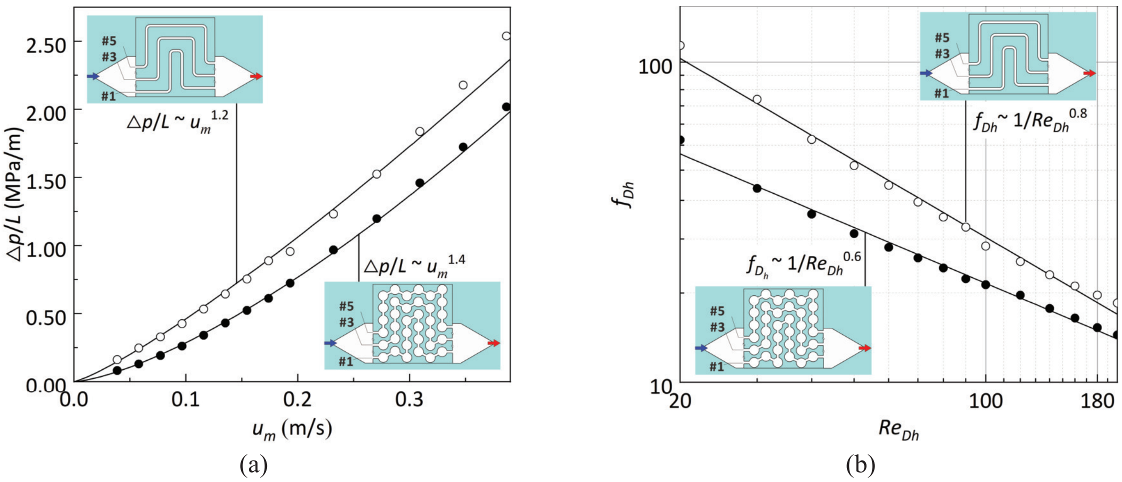

Fig. 8. Comparison of pressure drop between unmodified (reference) and cavitied cold plates. (a) Pressure drop per unit length. (b) Fanning friction factor.

considered, the pressure drop in the cavitied cold plate is reduced by 20%~50% with respect to the reference unmodified cold plate.

To generalize the dependence of pressure drop across a given cold plate on mean coolant velocity, the values are replotted in Fig. 8(b) using a fanning friction factor, f_{Dh}. The friction factor of the unmodified cold plate is empirically correlated as $f_{Dh} \sim 1/(\mathrm{Re}_{Dh})^{0.8}$, while $f_{Dh} \sim 1/(\mathrm{Re}_{Dh})^{0.6}$ holds for the cavitied cold plate. In the practical Reynolds number range of $\mathrm{Re}_{Dh} = 20 \sim 200$, the cavitied cold plate achieves, on average, ~30% lower flow resistance than its unmodified counterpart.

It is useful if both heat removal and pressure drop are considered simultaneously using a PEC, defined conventionally in (8) as PEC= $\mathrm{Nu}_{\mathrm{avg}}/f_{Dh}^{1/3}$. Results in Fig. 9(a) show that the cavitied cold plate provides almost doubled performance of its unmodified counterpart over the full Reynolds number range considered. A thermal performance parameter (η) defined by (9) the ratio of PEC for cavitied microchannel to that of unmodified microchannel [shown in Fig. 9(b)]. With this parameter, $\eta = 1.0$ indicates that the cavitied microchannel performs equally well as the unmodified microchannel, while $\eta = 2.0$ implies a 100% enhancement. With reference to Fig. 9(b), the cavitied microchannel results in an enhancement of 48%~169% (or on average 100%) over the Reynolds number range considered.

Notably, this thermal performance is much higher than that of a single straight, nonserpentine, microchannel [23], [24], [25], as well as multiple straight microchannels [26], [27]. As the Reynolds number is further increased, e.g., $\mathrm{Re}_{Dh} > 200$, the enhancement ratio due to sidewall modification in a serpentine cold plate is steeply decreased. It implies that the technological advantage with sidewall modification is only valid in multiple, serpentine flow paths in a low Reynolds number range. Fortunately, in the supposed practical Reynolds numbers of $20 \leq \mathrm{Re}_{Dh} \leq 200$, sidewall modification acts to enhance the cooling while reducing the pressure drop. Thus, for a given pumping power, more coolant can be pumped, leading to enhanced cooling.

B. Fluid Mechanisms Responsible for Enhanced Thermal Performance

For relatively low Reynolds numbers, a serpentine microchannel with sidewall modifications offers enhanced thermal performance over that of a straight microchannel, as seen in Fig. 9(b). It is assumed that the same mechanisms as those clarified for a straight microchannel cold plate [2] hold for the present cold plate. To justify this, at $\mathrm{Re}_{Dh} = 120$, μPIV was implemented for mapping the flow field within representative sidewall cavities in a transparent cold plate with 13 channel paths. Three of the paths (#1, #7, and #13) were specifically measured. Paths #1 and #13 exhibited some asymmetrical flow at their respective inlets, but no further distinctions were noted across the three. As such, only microchannel path #7 is presented here. Three locations along the path were selected, as seen in Fig. 10, representing: (I) inlet, (II) middle, and (III) outlet.

For a given cavity, the coolant is supplied to the cavity through an orifice-like straight throat ($t/D_h = 3.8$), t being the throat length and D_h the hydraulic diameter of the throat. At the cavity inlet, upon exiting the throat, the streamlines form a stream tube. This can be seen by (I) in Fig. 10(a) using the velocity contour based on the present μPIV measurements. As the coolant moves downstream from the cavity inlet, the coolant flow diffuses radially. Due to the relatively high static pressure at the cavity exit by contraction, the stream tube inflates radially along its mainstream immediately upstream of the exit. Limited by the outlet throat location with respect to the inlet throat location, the coolant follows the turning angle, e.g., $\theta = 28°$. A near mirror image of the streamlines is seen for case (III) featuring the same turning angle of $\theta = 28°$. For a representative cell in middle (II), the coolant enters the cavity from its top-left corner and leaves at the top-right corner, having a turning angle of $\theta = 56°$, as depicted. Such rapid turning causes a much earlier and wider inflation stream tube within the cavity compared to the case at inlet (I) for $\theta = 28°$. Finally, the coolant enters the drain chamber through a straight throat with a turning angle of $\theta = 28°$, as shown in (III) of Fig. 10(a).

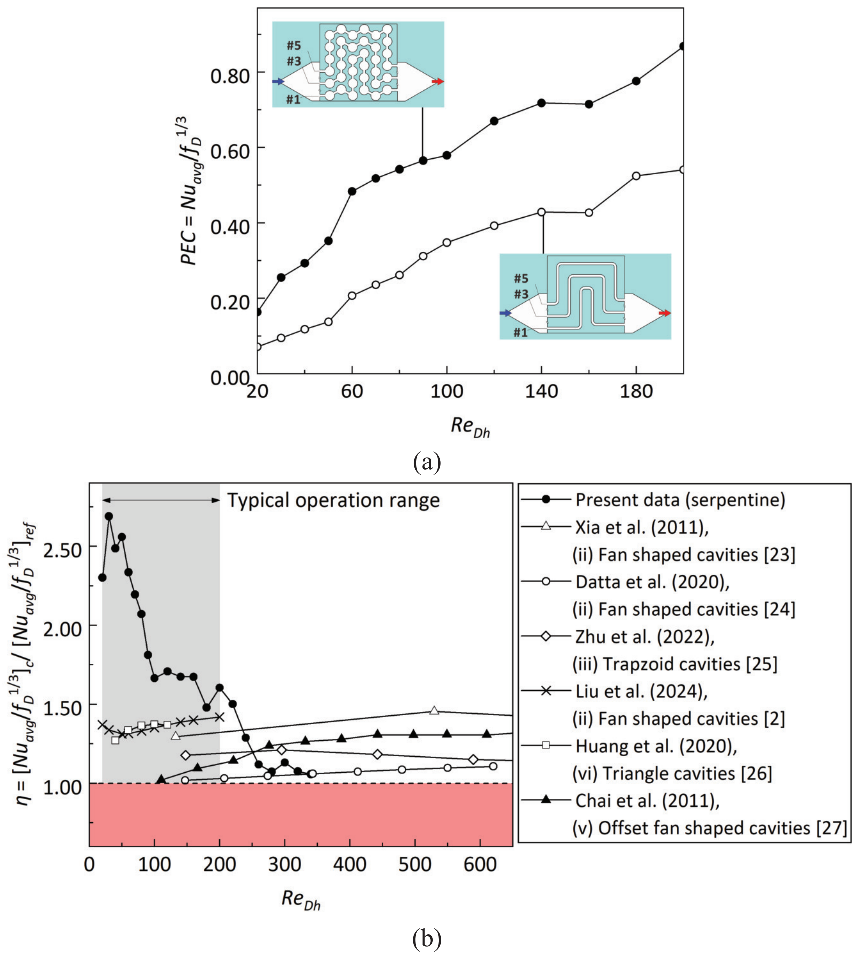

Fig. 9. Enhanced overall cooling by sidewall modification, with pressure drop considered. (a) PEC, defined by (8). (b) Comparison of thermal performance (η), defined by (9).

The vorticity contours shown in Fig. 10(b) indicate that the mixing of coolant is intensified within and near the throat, which plays a crucial role in improving the cooling performance within the throat and demands the presence of a cavity. Contraction of the streamline tube at cavity exit (throat inlet) results in increased mixing and the formation of a boundary layer in the throat. Then, bifurcation of the coolant flow at the cavity inlet (throat exit) causes another boundary layer to develop along the concave sidewalls of the cavity.

In summary, sidewall modification such as hemicircular cavities along straight microchannels reduces pressure drop: the stagnant fluid inside the cavities acts as a buffer layer between the mainstream and the cavities' concave sidewalls and; accordingly, flow slippage along the interface between the mainstream and stagnant fluid in such cavities acts to reduce the pressure drop compared to unmodified microchannels [22]. The same fluidic mechanisms hold for the reduced pressure drop achieved across serpentine microchannels in a cavitied cold plate. Furthermore, the intensified coolant mixing upstream, in each throat connecting successive sidewall cavities due to the redeveloping boundary layer, results in enhanced overall cooling in the cavitied cold plate, consistent with existing findings for a single straight microchannel cold plate [2].

It is worth noting that a fourth cavity case exists in two specific locations of the serpentine path, at the first and third turns of the path, where the turning angle is $\theta = 152°$. Such a turn is more excessive than those presented in Fig. 10 and may well result in notably different flow structures. However, in the present study, such cavities only feature twice in the channel path that features 50 cavities in total. It is therefore assumed that any unique flow structures present are negligible.

C. Improved Thermal Uniformity by Sidewall Modification and the Underlying Physical Mechanism

High thermal nonuniformity is an intrinsic problem with any serpentine cold plate design. The unmodified cold plate showcases such nonuniformity by contours (i)–(iv) of Fig. 7(a). These hotspots generate a thermal gradient across the cold plate, which is known to accelerate performance degradation of batteries or electronic chips [5], [6], [7]. In the current study, thermal uniformity of a given cold plate is evaluated using temperature deviation from a surface-averaged value, denoted as T_σ by (10). The variation of thermal uniformity with coolant Reynolds number is shown in Fig. 11 for both unmodified and cavitied microchannels. Quantitatively, the standard deviation of temperature distributions for both microchannels is $T_\sigma = \sim 7$ °C at $\mathrm{Re}_{Dh} = 0$ from $T_{s,m} = 100$ °C.

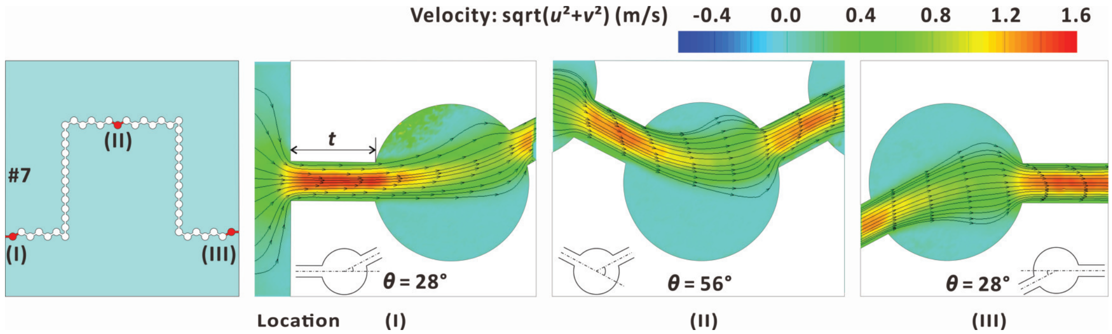

(a)

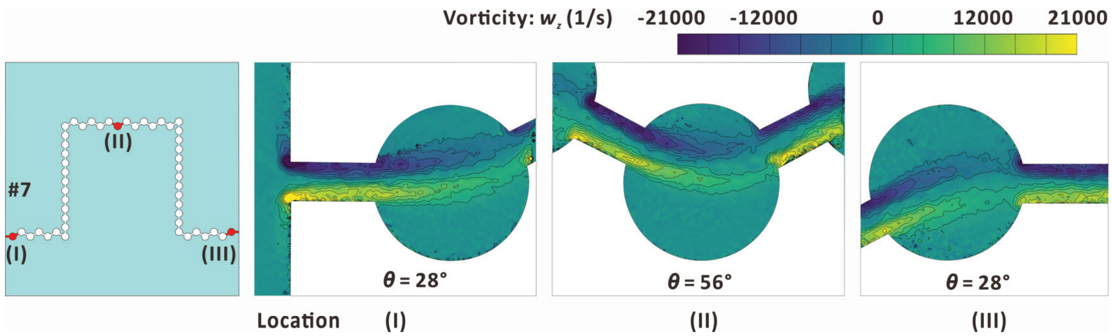

(b)

Fig. 10. Time-averaged flow field at selected regions (I at the inlet, II in the middle passage, and III at the outlet) for Channel #7 in a transparent microchannel cold plate, measured by μPIV at Re_{Dh} = 120. (a) Velocity contours and streamlines. (b) Vorticity.

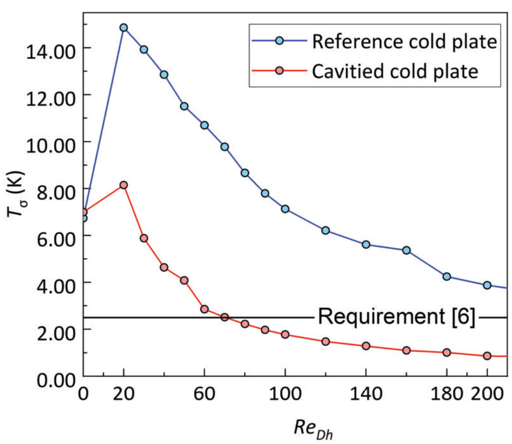

Fig. 11. Improved thermal uniformity by sidewall modification at Q_{input} = 6.8 W, indicated by the standard deviation of endwall temperatures varying with Reynolds number.

At $T_{f,\mathrm{in}}$ = 25 °C, thermal uniformity of the unmodified microchannel decreases monotonically from T_σ ~ 14.9 to 3.9 K, as seen in Fig. 11. For $\mathrm{Re}_{Dh} \leq 100$, the uniformity is worse than the cold plate without forced convection in the microchannels, i.e., $T_\sigma > 7.0$ K. The weak convection only acts to extend the hotspot region along microchannels that pass through the hotspot, as depicted in (ii) and (iii) of Fig. 7. As the Reynolds number is increased further to Re_{Dh} = 200, the heated coolant is now drained at a faster rate. Thus, the cold plate becomes more uniform as shown by contour (iv) in Fig. 7. It corresponds to a smaller standard deviation than that without convection, e.g., $T_\sigma < 7.0$ K. Notably, such uniformity does not satisfy the uniformity requirement for battery cooling (i.e., T_σ = 2.5 K [6]).

For the cavitied microchannel, the thermal uniformity similarly increases monotonically (i.e., T_σ decreases) but with lower values: from T_σ ~ 8.2 to 0.9 K. With forced convection in a cavitied serpentine microchannel, thermal uniformity is better than the case without convection, as can be seen in contours (v)–(viii) in Fig. 7 for $\mathrm{Re}_{Dh} > 30$. Furthermore, for $\mathrm{Re}_{Dh} > 60$, the standard deviation becomes lower than the requirement for battery cooling (T_σ = 2.5 K [6]). In comparison to the reference cold plate, the cavitied cold plate substantially reduces (improves) thermal uniformity by 45.2%~77.7%. Over the Reynolds number range considered, an average improvement of 70% is achieved.

The mechanism for such an improvement to thermal uniformity can be considered using a simple thermal resistance model for straight microchannel cold plates (with and without sidewall modifications), as illustrated in Fig. 12(a). Each cold plate had a width of W = 10 mm and a length of L = 54 mm. The cross section of the unmodified microchannel is circular, with its inner diameter D = 500 μm. For the cavitied cold plate, 19 cylindrical cavities with a diameter of D_c = 2.0 mm are aligned along the straight microchannel (D = 500 μm), with the center-to-center spacing fixed at d_1 = 2.5 mm. Numerical results used in the model are based on those detailed in a previous study [2].

For steady-state heat transfer in a given cold plate, heat is transferred from the source attached to the substrate via conduction, subsequently removed by convection in the microchannels. Both conduction and convection are coupled to

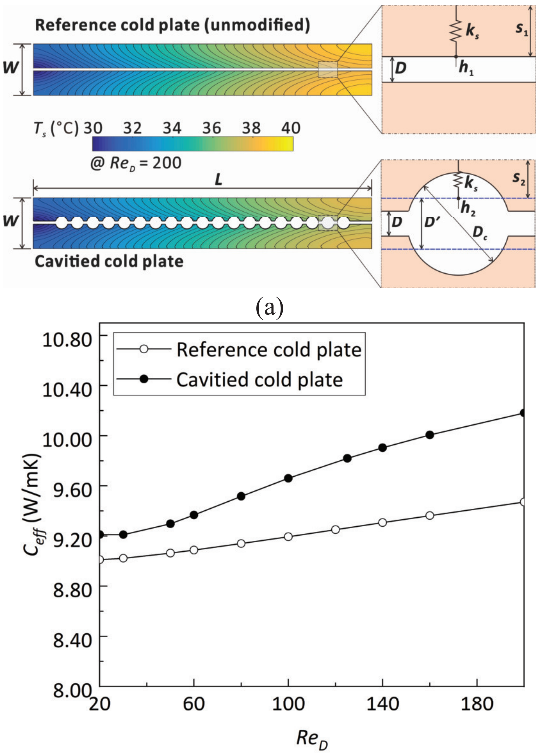

Fig. 12. Effective conductance of both reference and cavitied microchannel cold plates. (a) Schematic of a conductance model. (b) Comparison and variation of effective conductance (C_{eff}) with Reynolds number.

determine the thermal uniformity of the cold plate. Based on thermal resistances in series [39], the overall thermal resistance per unit length may be expressed as

$$R_{\text{total}} = R_{\text{cond}} + R_{\text{conv}} \tag{12}$$

where $R_{\text{cond}} = 1/k_s$ is the thermal resistance of conduction, $R_{\text{conv}} = 1/(h \times s)$ is the thermal resistance of convection, k_s is the thermal conductivity of the substrate, h is the area-averaged heat transfer coefficient, and s is the spreading distance for a microchannel. Effective thermal conductance is now expressed as the inverse of overall thermal resistance [39] as

$$C_{\text{eff}} = \frac{1}{R_{\text{total}}} = \frac{k_s hs}{k_s + hs}. \tag{13}$$

For an unmodified cold plate, the effective thermal conductance is expressed as

$$C_{\text{eff},1} = \frac{k_s h_1 s_1}{k_s + h_1 s_1} \tag{14}$$

where k_s is the thermal conductivity of the substrate, h_1 is the area-averaged heat transfer coefficient, and $s_1 = (W - D)/2$ is the distance from the microchannel wall to the edge of the cold plate. The cavitied cold plate is equivalent to an unmodified cold plate having the same overall dimensions. Due to the presence of cavities, there is a larger equivalent microchannel diameter (i.e., $D' = 0.88$ mm) representing an unmodified microchannel, as shown in Fig. 12(a). Therefore, it shortens the conductive path compared to the reference cold plate. The effective thermal conductance can be derived as

$$C_{\text{eff},2} = \frac{k_s h_2 s_2}{k_s + h_2 s_2} \tag{15}$$

where h_2 is the area-averaged heat transfer coefficient and $s_2 = (W - D')/2$ is the distance from the equivalent microchannel wall to the edge of the cold plate, as shown by the inset of Fig. 12(a).

In the Reynolds number range of $\text{Re}_D = 20 \sim 200$, the effective thermal conductance of both cold plate types increases with increasing Reynolds number, due mainly to enhanced convection, as displayed in Fig. 12(b). Compared to the reference cold plate, the effective thermal conductance is enhanced by wall modification up to ~7.5%. This is attributed to enhanced local convection and shortened conductive path by wall modification. Therefore, the increased thermal conductance by wall modification explains the improved thermal uniformity observed in Fig. 11.

IV. Conclusion

A cold plate design that can mitigate thermal nonuniformity with enhanced overall cooling has been envisioned, which arranges hemicircular cavity cells along serpentine microchannels, leading to a cavitied cold plate. To confirm the effectiveness of such a design, a series of thermofluidic characterizations on both reference and cavitied cold plates, subjected to constant heat flux, were carried out by IR thermography as well as pressure and velocity measurements, within a practical Reynolds number range of $20 \leq \text{Re}_{Dh} \leq 200$. The cavitied cold plate design provided about 70% improved thermal uniformity over the reference cold plate, mainly due to increased effective conductance by both elevated local convection and shortened conductive path. Furthermore, the cavitied cold plate gave rise to approximately 76% enhanced overall cooling and 50% reduced pressure drop at a given flow rate. As a result, with pumping power fixed, the thermal performance is further enhanced: ~100% better cooling than the reference cold plate. The proposed cold plate design provides an alternative option for thermally managing semiconductor chips and/or Li-ion batteries that simultaneously require improved thermal uniformity and enhanced overall cooling.

References

[1] D. R. Weber, S. J. Spencer, and P. F. Spacher, "*Battery cooling plate design with discrete channels*," U.S. Patent 7851080 B2, Dec. 14, 2010.

[2] Y. Liu, S. W. Schekman, K. Zhang, T. J. Lu, and T. Kim, "Mechanisms of enhanced cooling by sidewall modification in a microtube cold plate," *ASME J. Heat Mass Transf.*, vol. 147, no. 4, Apr. 2025, Art. no. 041801.

[3] C. G. Motloch et al., "High-power battery testing procedures and analytical methodologies for HEV's," in *Proc. SAE Tech. Paper Ser.*, Jun. 2002, pp. 797–802.

[4] A. Väyrynen and J. Salminen, "Lithium ion battery production," *J. Chem. Thermodyn.*, vol. 46, pp. 80–85, Mar. 2011.

[5] S. Li, C. Zhang, Y. Zhao, G. J. Offer, and M. Marinescu, "Effect of thermal gradients on inhomogeneous degradation in lithium-ion batteries," *Commun. Eng.*, vol. 2, no. 1, pp. 1–14, Oct. 2023.

[6] A. Greco, X. Jiang, and D. Cao, "An investigation of lithium-ion battery thermal management using paraffin/porous-graphite-matrix composite," *J. Power Sources*, vol. 278, pp. 50–68, Mar. 2015.

[7] Z. He, Y. Yan, and Z. Zhang, "Thermal management and temperature uniformity enhancement of electronic devices by micro heat sinks: A review," *Energy*, vol. 216, Feb. 2021, Art. no. 119223.

[8] M. E. Steinke and S. G. Kandlikar, "Single-phase heat transfer enhancement techniques in microchannel and minichannel flows," in *Proc. ASME 2nd Int. Conf. Microchannels Minichannels*, New York, NY, USA, Jan. 2004, pp. 141–148.

[9] S. G. Kandlikar, S. Joshi, and S. Tian, "Effect of surface roughness on heat transfer and fluid flow characteristics at low Reynolds numbers in small diameter tubes," *Heat Transf. Eng.*, vol. 24, no. 3, pp. 4–16, May 2003.

[10] M. Everts, P. Robbertse, and B. Spitholt, "The effects of surface roughness on fully developed laminar and transitional flow friction factors and heat transfer coefficients in horizontal circular tubes," *Int. J. Heat Mass Transf.*, vol. 189, Jun. 2022, Art. no. 122724.

[11] N. R. Rosaguti, D. F. Fletcher, and B. S. Haynes, "Laminar flow and heat transfer in a periodic serpentine channel with semi-circular cross-section," *Int. J. Heat Mass Transf.*, vol. 49, nos. 17–18, pp. 2912–2923, Aug. 2006.

[12] N. R. Rosaguti, D. F. Fletcher, and B. S. Haynes, "Laminar flow and heat transfer in a periodic serpentine channel," *Chem. Eng. Technol.*, vol. 28, no. 3, pp. 353–361, Mar. 2005.

[13] H. M. Jaffal, N. S. Mahmoud, A. A. Imran, and A. Hasan, "Performance enhancement of a novel serpentine channel cooled plate used for cooling of Li-ion battery module," *Int. J. Thermal Sci.*, vol. 184, Feb. 2023, Art. no. 107955.

[14] S. G. Kandlikar and W. J. Grande, "Evaluation of single phase flow in microchannels for high heat flux chip cooling—Thermohydraulic performance enhancement and fabrication technology," *Heat Transf. Eng.*, vol. 25, no. 8, pp. 5–16, Dec. 2004.

[15] S. Zhang, F. Ahmad, A. Khan, N. Ali, and M. Badran, "Performance improvement and thermodynamic assessment of microchannel heat sink with different types of ribs and cones," *Sci. Rep.*, vol. 12, no. 1, Jun. 2022, Art. no. 1.

[16] C. A. Rubio-Jimenez, S. G. Kandlikar, and A. Hernandez-Guerrero, "Numerical analysis of novel micro pin fin heat sink with variable fin density," *IEEE Trans. Compon., Packag., Manuf. Technol.*, vol. 2, no. 5, pp. 825–833, May 2012.

[17] J. Barrau, M. Omri, D. Chemisana, J. Rosell, M. Ibañez, and L. Tadrist, "Numerical study of a hybrid jet impingement/micro-channel cooling scheme," *Appl. Thermal Eng.*, vols. 33–34, pp. 237–245, Feb. 2012.

[18] G. Xie, Z. Chen, B. Sunden, and W. Zhang, "Numerical analysis of flow and thermal performance of liquid-cooling microchannel heat sinks with bifurcation," *Numer. Heat Transf., A, Appl.*, vol. 64, no. 11, pp. 902–919, Dec. 2013.

[19] M. K. Patterson, X. Wei, Y. Joshi, and R. Prasher, "Numerical study of conjugate heat transfer in stacked microchannels," in *Proc. 9th Intersociety Conf. Thermal Thermomechanical Phenomena Electron. Syst.*, Jun. 2004, pp. 372–380.

[20] M.-C. Lu and C.-C. Wang, "Effect of the inlet location on the performance of parallel-channel cold-plate," *IEEE Trans. Compon. Packag. Technol.*, vol. 29, no. 1, pp. 30–38, Mar. 2006.

[21] J. Shen, Y. Wang, G. Yu, and H. Li, "Thermal management of prismatic lithium-ion battery with minichannel cold plate," *J. Energy Eng.*, vol. 146, no. 1, Feb. 2020, Art. no. 04019033.

[22] Y. Liu, S. W. Schekman, M. Li, T. Lu, and T. Kim, "Transitional pressure drop in a cavitied microchannel," *Phys. Rev. Fluids*, vol. 9, no. 4, Apr. 2024, Art. no. 044201.

[23] G. Xia, L. Chai, M. Zhou, and H. Wang, "Effects of structural parameters on fluid flow and heat transfer in a microchannel with aligned fan-shaped reentrant cavities," *Int. J. Thermal Sci.*, vol. 50, no. 3, pp. 411–419, Mar. 2011.

[24] A. Datta, D. Debbarma, N. Biswas, D. Sanyal, and A. K. Das, "The role of flow structures on the thermal performance of microchannels with wall features," *J. Thermal Sci. Eng. Appl.*, vol. 13, no. 2, Apr. 2021, Art. no. 021019.

[25] Q. Zhu et al., "Heat transfer enhancement for microchannel heat sink by strengthening fluids mixing with backward right-angled trapezoidal grooves in channel sidewalls," *Int. Commun. Heat Mass Transf.*, vol. 135, Jun. 2022, Art. no. 106106.

[26] B. Huang, H. Li, S. Xia, and T. Xu, "Experimental investigation of the flow and heat transfer performance in micro-channel heat exchangers with cavities," *Int. J. Heat Mass Transf.*, vol. 159, Oct. 2020, Art. no. 120075.

[27] L. Chai, G. Xia, M. Zhou, and J. Li, "Numerical simulation of fluid flow and heat transfer in a microchannel heat sink with offset fan-shaped reentrant cavities in sidewall," *Int. Commun. Heat Mass Transf.*, vol. 38, no. 5, pp. 577–584, May 2011.

[28] M. Raffel, C. E. Willert, F. Scarano, C. J. K?hler, S. T. Wereley, and J. Kompenhans, "Micro-PIV," in *Particle Image Velocimetry: A Practical Guide*, 3rd ed., Berlin, Germany: Springer, 2018, pp. 367–412.

[29] R. J. Adrian and J. Westerweel, "Microscopic system," in *Particle Image Velocimetry*. New York, NY, USA: Cambridge Univ. Press, 2011, pp. 205–217.

[30] M. G. Olsen and R. J. Adrian, "Out-of-focus effects on particle image visibility and correlation in microscopic particle image velocimetry," *Experim. Fluids*, vol. 29, no. 7, pp. S166–S174, Dec. 2000.

[31] C. D. Meinhart, S. T. Wereley, and M. H. B. Gray, "Volume illumination for two-dimensional particle image velocimetry," *Meas. Sci. Technol.*, vol. 11, no. 6, pp. 809–814, May 2000.

[32] R. L. Webb, "Performance evaluation criteria for use of enhanced heat transfer surfaces in heat exchanger design," *Int. J. Heat Mass Transf.*, vol. 24, no. 4, pp. 715–726, Apr. 1981.

[33] R. L. Webb and N.-H. Kim, "Performance evaluation criteria for sing-phase flow," in *Principles Enhanced Heat Transfer*, 2nd ed., New York, NY, USA: Garland Science, 2004, pp. 55–74.

[34] H. W. Coleman and W. G. Steele, *Experimentation, Validation, and Uncertainty Analysis for Engineers*, 3rd ed., Hoboken, NJ, USA: Wiley, 2018.

[35] J. G. Santiago, S. T. Wereley, C. D. Meinhart, D. J. Beebe, and R. J. Adrian, "A particle image velocimetry system for microfluidics," *Experim. Fluids*, vol. 25, no. 4, pp. 316–319, Sep. 1998.

[36] A. K. Prasad, R. J. Adrian, C. C. Landreth, and P. W. Offutt, "Effect of resolution on the speed and accuracy of particle image velocimetry interrogation," *Experim. Fluids*, vol. 13, nos. 2–3, pp. 105–116, Jun. 1992.

[37] J. Westerweel, "On velocity gradients in PIV interrogation," *Experim. Fluids*, vol. 44, no. 5, pp. 831–842, May 2008.

[38] J. Westerweel, "Theoretical analysis of the measurement precision in particle image velocimetry," *Experim. Fluids*, vol. 29, no. 7, pp. S003–S012, Dec. 2000.

[39] T. L. Bergman, A. S. Lavine, F. P. Incropera, and D. P. Dewitt, *Fundamentals of Heat and Mass Transfer*, 7th ed., Hoboken, NJ, USA: Wiley, 2011, pp. 517–568.

[40] G. L. Morini, "Viscous dissipation as scaling effect for liquid flows in microchannels (Keynote)," in *Proc. ASME 3rd Int. Conf. Microchannels Minichannels*, A B, Ontario, ON, Canada, Jun. 2005, pp. 93–102.

[41] G. Maranzana, I. Perry, and D. Maillet, "Mini- and micro-channels: Influence of axial conduction in the walls," *Int. J. Heat Mass Transf.*, vol. 47, nos. 17–18, pp. 3993–4004, Aug. 2004.

[42] G. Maranzana, I. Perry, and D. Maillet, "Conjugated heat transfer in 2-dimensional mini and micro channels: Influence of axial conduction in the walls," in *Proc. ASME 2nd Int. Conf. Microchannels Minichannels*, New York, NY, USA, Jan. 2004, pp. 251–258.

[43] B. R. Munson, T. H. Okiishi, W. W. Huebsch, and A. P. Rothmayer, "Viscous flow in pipes," in *Fundamentals of Fluid Mechanics*, 7th ed., Hoboken, NJ, USA: Wiley, 2012, pp. 400–479.

Yanyan Liu received the B.Sc. degree in aerospace design from Nanjing University of Aeronautics and Astronautics (NUAA), Nanjing, China, in 2019, where he is currently pursuing the Ph.D. degree in microfluidics for electronics cooling.

Since 2018, he has been with the MIIT Key Laboratory of Multifunctional Lightweight Materials and Structures and the College of Aerospace Engineering, NUAA. His research focuses on thermofluidic measurement techniques in microscale, pulsatile flow in microfluidic biomedical and electronic devices.

Sjouke Willem Schekman was born in Durban, South Africa, in May 1988. He received the B.Sc. degree in aeronautical engineering from the University of the Witwatersrand, Johannesburg, South Africa, in 2010, the M.Sc. degree in engineering from the University of the Witwatersrand in 2015, with a focus on aircraft aileron design, and the Ph.D. degree from the University of the Witwatersrand in 2024, with a focus on investigating gas turbine blade cooling configurations.

While undertaking his M.Sc. degree, he began to work in 2012 as an Associate Lecturer at the School of Mechanical, Industrial and Aeronautical Engineering, University of the Witwatersrand. He was promoted to a Lecturer in 2015 and the Head of Design in 2020. He has authored and co-authored publications on the thermofluidic performance of pin-fin cooling, impinging jets, and, more recently, microfluidics. His current research interests are focused on jet flows and microfluidics.

Dr. Schekman is a member of the Royal Aeronautical Society.

Yongpu Wang received the B.Sc. degree in mechanical engineering from Xiangtan University, Xiangtan, China, in 2018, and the M.Sc. degree from Nanjing University of Aeronautics and Astronautics (NUAA), Nanjing, China, in 2022, where he is currently pursuing the Ph.D. degree with the MIIT Key Laboratory of Multifunctional Lightweight Material and Structures and the College of Aerospace Engineering.

His research interests are in developing a wind energy harnessing technology for off-grid sensing and monitoring devices and in solid–fluid coupling due to thermal and momentum gradients.

Tian Jian Lu received the B.Sc. and M.Sc. degrees in applied mechanics from Xi'an Jiaotong University (XJTU), Xi'an, China, in 1984 and 1987, respectively, and the Ph.D. degree in engineering sciences from Harvard University, Cambridge, MA, USA, in 1995.

He was a Chair Professor of materials engineering at the University of Cambridge, Cambridge, U.K. He is a Professor with the College of Aerospace Engineering, Nanjing University of Aeronautics and Astronautics (NUAA), Nanjing, China, and holds jointly a Professorship at the School of Aerospace Engineering, XJTU. He is also the Founding Director of the MIIT Key Laboratory of Multifunctional Lightweight Materials and Structures, NUAA, and the Biomedical Engineering and Biomechanics Center, XJTU. His research focuses on challenges in mechanics of materials, noise and vibration, heat transfer, and biomechanics.

Dr. Lu is a fellow of American Institute for Medical and Biological Engineering.

Tongbeum Kim received the B.Eng. degree in mechanical engineering from Kyung Hee University, Seoul, South Korea, in 1997, the M.Sc. degree in aerospace engineering from Georgia Institute of Technology, Atlanta, GA, USA, in 1998, and the Ph.D. degree in aerothermal technology from the University of Cambridge, Cambridge, U.K., in 2004.

He was a Chair Professor with the School of Mechanical, Industrial and Aeronautical Engineering, University of the Witwatersrand, Johannesburg, South Africa. He is a Professor with the College of Aerospace Engineering, Nanjing University of Aeronautics and Astronautics, Nanjing, China. His research focuses on the growing concerns over sustainability, primarily through the thermal management of various sustainable/renewable energy generation and storage systems.

Dr. Kim is a member of the Royal Aeronautical Society.